Narrow River Extraction From SAR Images Using Exogenous Information

Nicolas Gasnier [ID] , *Student Member, IEEE*, Loïc Denis [ID] , Roger Fjørtoft [ID] , *Member, IEEE*, Frédéric Liège, and Florence Tupin [ID] , *Senior Member, IEEE*

Abstract—Monitoring of rivers is of major scientific and societal importance due to the crucial resource they provide to human activities and the threats caused by flood events. Rapid revisit synthetic aperture radar (SAR) sensors such as Sentinel-1 or the future surface water and ocean topography (SWOT) mission are indispensable tools to achieve all-weather monitoring of water bodies at the global scale. Unfortunately, at the spatial resolution of these sensors, the extraction of narrow rivers is extremely difficult without resorting to exogenous knowledge. This article introduces an innovative river segmentation method from SAR images using *a priori* databases such as the global river widths from Landsat (GRWL). First, a recently proposed linear structure detector is used to produce a map of likely line structures. Then, a limited number of nodes along the prior river centerline are extracted from the exogenous database and used to reconstruct the full river centerline from the detection map. Finally, an innovative conditional random field approach is used to delineate accurately the river extent around its centerline. The proposed method has been tested on several Sentinel-1 images and on simulated SWOT data. Both visual and qualitative evaluations demonstrate its efficiency.

Index Terms—Conditional random field (CRF), graph cut, hydrology, river extraction, segmentation, synthetic aperture radar (SAR).

I. INTRODUCTION

IN THE last five years, two major research works have provided comprehensive worldwide maps of continental water surfaces: the global surface water masks of Pekel *et al.* [1] and global river widths from Landsat (GRWL) of Allen and Pavelsky [2]. They are based on multispectral Landsat optical images over decades. Such optical satellite sensors are not well suited for real-time monitoring of water bodies, as they lack the all-weather capability of synthetic aperture radar (SAR) sensors such as Sentinel-1 that can observe through clouds. The Ka-band radar interferometer (KaRIn) of the future surface water and ocean topography (SWOT) mission [3], scheduled for launch in 2022, is an interferometric SAR system that is able to measure water elevation as well. Thanks also to their short revisit time, these freely available SAR data are expected to play a crucial role in river monitoring in the coming years. However, SAR images have specific characteristics that make their direct exploitation difficult. In addition to their limited number of information channels, these images are corrupted by strong multiplicative speckle noise and affected by artifacts that can make their exploitation for water detection difficult. Robust and efficient methods to detect narrow rivers in such images are therefore needed.

Most of the methods previously developed for river detection do not use exogenous information, except for some approaches using digital earth models to account for slope in water detection both with SAR and optical images [4]. Multiple generic water detection algorithms, not specific to rivers, have already been proposed, for example, by Liu and Jezek [5] or Cazals *et al.* [6], which applies thresholding on a filtered SAR image or the baseline method for operational water detection in SWOT images of Lobry *et al.* [7] that uses Markov random fields (MRF). Other methods use active contour approaches such as level sets [8]. These methods use strong regularization priors to avoid speckle-induced false detection, which impairs the detection of narrow rivers. Specific approaches for river detection have also been proposed such as the one developed by Cao *et al.* [9] for SWOT images. Valero [10] proposes an approach based on mathematical morphology for road detection in high-resolution images. This approach has been adapted for rivers and automated using machine learning by Klemenjak *et al.* [11]. Sghaier *et al.* [12] combine it with structural feature sets. Other approaches based on active contours have also been used, such as [13].

The detection of narrow rivers in SAR images with a limited false detection rate is very difficult without using any exogenous information. Indeed, beyond usual issues associated with speckle noise and low contrast, river detection is particularly complex because roads, terrain slope, and various artifacts can create structures resembling rivers such as in Fig. 1. Distinguishing rivers from other visually similar structures such as the large road in Fig. 1(a) or the topography artifact in Fig. 1(b) can be very

Nicolas Gasnier is with the LTCI, Télécom Paris, Institut Polytechnique de Paris, 91120 Palaiseau, France, and also with the CS Group - France, 31500 Toulouse, France (e-mail: nicolas.gasnier@telecom-paris.fr).

Loïc Denis is with the Univ Lyon, UJM-Saint-Etienne, CNRS, Institut d Optique Graduate School, Laboratoire Hubert Curien UMR 5516, F-42023, SAINT-ETIENNE, France (e-mail: loic.denis@univ-st-etienne.fr).

Florence Tupin is with the LTCI, Télécom, Institut Polytechnique de Paris, 91120 Palaiseau, France (e-mail: Florence.tupin@telecom-paris.fr).

Roger Fjørtoft is with the Centre National d'Études Spatiales, 31401 Toulouse, France (e-mail: roger.fjortoft@cnes.fr).

Frédéric Liège is with the CS Group - France, 31500 Toulouse, France (e-mail: frederic.liege@csgroup.eu).
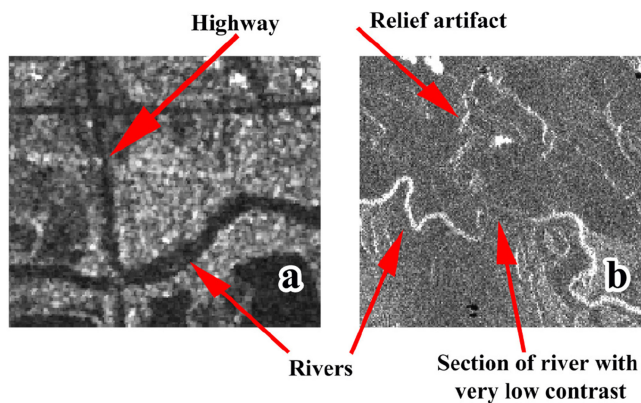
Fig. 1. Crop of (a) Sentinel-1 image from Des Moines and (b) simulated SWOT image (Saline), presented in Section III. Both images contain linear structures that correspond to actual rivers and linear structures that correspond to other structures: a large road for (a) and terrain slope layover effects for (b). Image (b) also shows a river section with very low contrast.
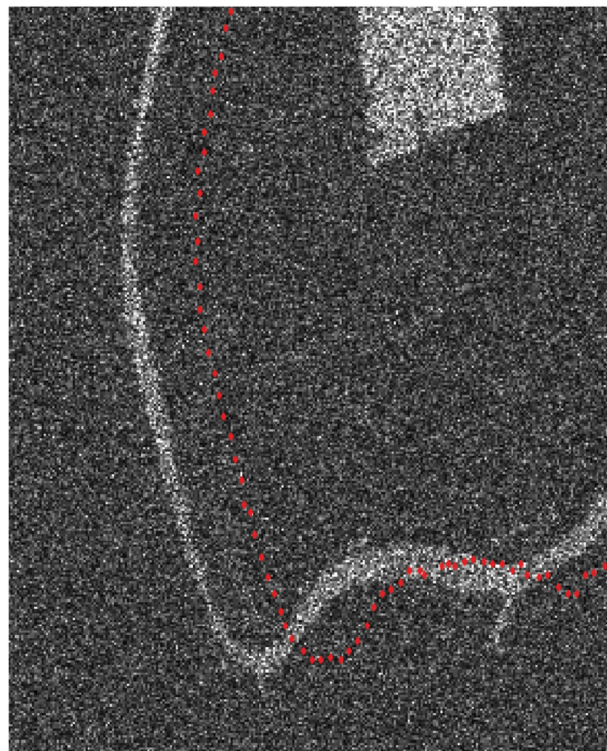

Fig. 2. Illustration of the displacement between the database centerline projected in radar geometry (red dotted line) and the river observed in a simulated SWOT image (where water is bright and land is dark). Such a displacement can be caused by variations in water elevation and inaccuracies in the digital elevation model used for projection: a few meters difference between actual and prior elevation can lead to shifts of hundreds of meters in ground range.

difficult or even impossible when using only the information available in the image, especially when the contrast of an actual river can be very low [as in Fig. 1(b)]. To prevent false detection, prior information about the location and the direction of known rivers can be useful. It allows distinguishing linear structures corresponding to a known river from other visually similar linear features. For example, rough waypoints from exogenous data can give information about the course of the river that has to be detected.

In this context, the aforementioned GRWL database provides, on a global scale, information that can be included within new approaches for river detection from SAR images. Before such global databases became available, the use of exogenous information was difficult and often required manual preparation of input and semiautomated approaches, such as [14] and [15] for optical images. In contrast, GRWL contains a centerline for each river that provides information about the course of the river. If this database centerline did perfectly correspond to the actual river centerline in the image after projection to the image coordinates, its use would be straightforward and only the third step of the proposed method would be needed. Unfortunately, direct use of the prior centerline of a river provided by the database to detect and segment the river in a SAR image remains problematic. Indeed, there are three main reasons as to why there can be a discrepancy between the database centerline projection in the image and the actual river.

1) The actual position and shape of the river can evolve over time [16], especially for meandering rivers [17]. Such changes can be very quick in case of major flood events or earthquakes or when caused by human activity. Rivers can also undergo seasonal changes that the database does not take into account.

2) There can be a positional error caused by the projection of the database centerline into the radar image. For Sentinel-1 ground range detected (GRD) images, it can be induced by the GRD image construction or orthorectification process

[inaccurate digital elevation model (DEM) or errors in the water level]. For SWOT images, as the water detection is done in radar geometry and before water height extraction, shifts could come from a difference between the prior water level used for the projection of the centerline and the actual water level. The near-nadir geometry of SWOT is very sensitive to this, as even a relatively small difference in elevation can lead to a major shift in position in the range direction as illustrated in Fig. 2.

3) There may be some errors in the database itself, especially in areas with complex topology or dense vegetation.

This brings the need for an approach that can exploit the exogenous information provided by GRWL's river centerlines while being robust to discrepancies between the projection of these centerlines and the true river in the image. We, therefore, propose a robust approach that uses the database centerlines as a source of approximate waypoints that can be used in combination with the image to retrieve the actual river centerline. This centerline can then be used to accurately detect the river extent while avoiding confusion with other linear structures.

The main contribution of this article is to propose a new river detection approach for SAR images, guided by prior information on the approximate river location. It can be provided by a database such as GRWL that features several information layers
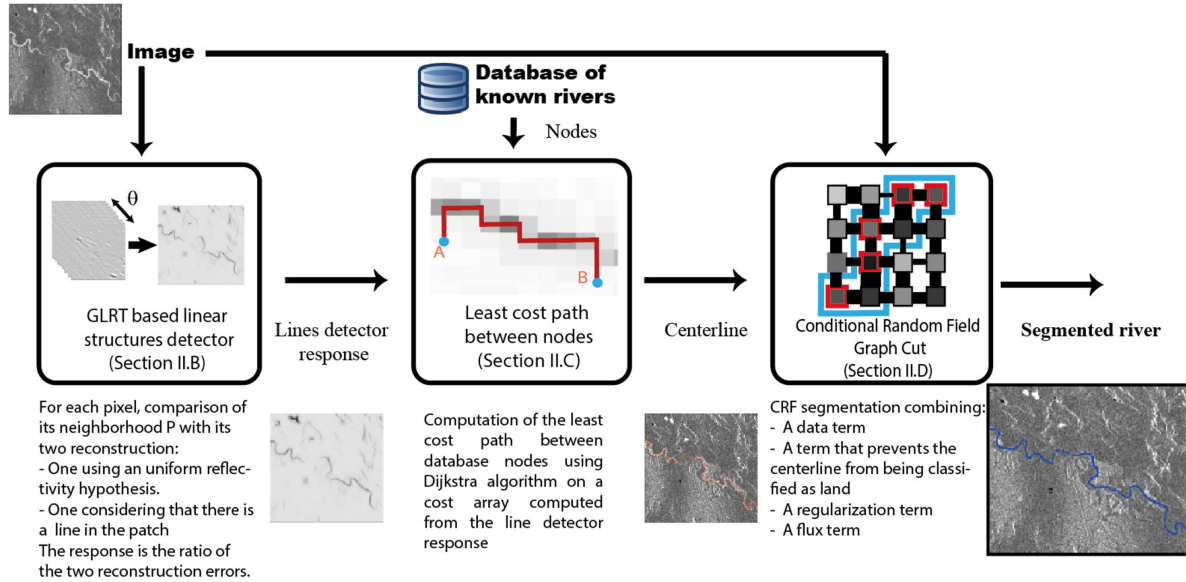
Fig. 3. Global overview of the proposed method: The first step consists in computing the linear structure detector response, used in the second step with the nodes from the *a priori* database to retrieve the centerline. The river is then segmented around the centerline using a CRF approach in the third step.

including the river centerline for most rivers wider than 30 m, with better completeness for rivers above 90 m. The robustness and efficiency of the proposed method are illustrated by several examples for both Sentinel-1 and simulated SWOT data. The article is organized as follows: The method is presented in Section II, the results are presented and discussed in Section III, and conclusion and future work are detailed in Section IV.

II. PROPOSED FRAMEWORK

A. Overview

As mentioned in Section I, our goal is to provide a novel framework for river extraction in SAR images using a database of rivers to overcome the limitations of detection based only on an SAR image. The method needs to be robust to differences between the observed river location and shape and those in the database. To achieve this, we propose a three-step framework summarized in Fig. 3. The first step consists in applying a line detector to the SAR image, as described in the next section. Its response gives the likelihood of the presence of a locally linear structure at each pixel of the image, irrespective of the nature of the linear structure (river, road, artifact, etc.). The second step uses the Dijkstra algorithm [18] to find the least-cost curvilinear path between two nodes of the prior river database through a cost array derived from the response of the linear structure detector. These first two steps lead to an estimation of the actual river centerline in the image that is robust to speckle noise and low water/land contrast and to inaccuracies in the shape and position of the prior centerline projected in radar geometry. The third step consists in segmenting the river reach around the extracted centerline to accurately delineate the river extent (width). An innovative conditional random field (CRF) approach is proposed for this purpose.

B. Detection of Linear Structures in the SAR Image

The first step of our approach computes a map that indicates the likelihood of the presence of a linear structure at each pixel of the image. In our context, a linear structure can be defined as a set of contiguous pixels in a long and thin layout (width of a few pixels) whose radar reflectivity (brightness) is significantly different from that of the background [19]. The relevant linear structures can be dark, as for most sensors such as Sentinel-1 or RADARSAT, or bright for near-nadir sensors such as KaRIn on the future SWOT satellite. The detection of lines on SAR images can be very difficult because of the strong, multiplicative speckle noise and the low contrast of some rivers. Therefore, methods developed for optical images [20]–[24] cannot be directly applied to SAR images, even after log-transformation to make the speckle additive. Methods specific to SAR images have been proposed in the past by Hellwich *et al.* [25], who use both intensity and coherence images, and by Tupin *et al.* [26] who combine the results of two detectors: one based on ratios in a neighborhood and the other based on cross-correlation. More recently, the authors have developed a line detector that improved the detection performance compared to [26] and has been described and tested in [19].

As explained in [19], this detector is based on a generalized likelihood ratio test (GLRT) and evaluates at each pixel k the likelihood ratio between two hypotheses on a small square patch $\boldsymbol{I}_\square(k)$ of size $(2N+1) \times (2N+1)$ centered on the considered pixel k:

1) H_0: absence of any linear structure (homogeneous area);
2) H_1: presence of a linear structure.

The GLRT at pixel k can be written as

$$\text{GLRT}(k) = \frac{\text{p}(\widetilde{\boldsymbol{I}}(k)|H_1, \widehat{\boldsymbol{P}}(k), \widehat{\theta(k)})}{\text{p}(\widetilde{\boldsymbol{I}}(k)|H_0, \widehat{R}(k))}. \tag{1}$$
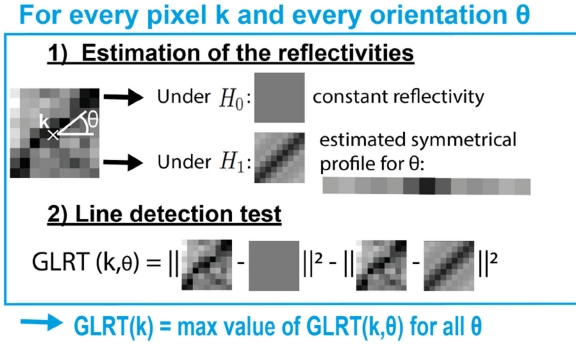
Fig. 4. General presentation of the linear structures detection performed on the log-transformed images. Example for a patch centered in k and for dark linear structure detection.

$\widetilde{I}(k)$ is a vector obtained by concatenating the log-transformed intensities of every pixels of the patch $I_\square(k)$.

For both hypotheses, the likelihood depends on unknown parameters that can be estimated by maximum likelihood. Under the H_0 hypothesis, the only parameter is the homogeneous reflectivity $R(k)$ over the patch $I_\square(k)$, whose estimator is $\widehat{R}(k)$. Under the H_1 hypothesis, there are two parameters: the orientation of the line $\theta(k)$ and the estimated profile $P(k)$, which is a vector containing the intensities along the direction perpendicular to the line. With our model, this profile is symmetric and its extreme value is located in its center (see Fig. 4).

The GLRT presented in (1) can be simplified by considering a Gaussian approximation of the log-transformed speckle [27] which leads to the quadratic expression

$$p(\widetilde{I}|\widetilde{R}_\mu) \simeq f(\widetilde{I}) = \frac{1}{\sigma\sqrt{2\pi}}\,e^{-\frac{1}{2}\left(\frac{\widetilde{I}-\widetilde{R}_\mu}{\sigma}\right)^2} \qquad (2)$$

where $\sigma = \sqrt{\psi(1,L)}$, $\widetilde{R}_\mu = \widetilde{R} - \log(L) + \psi(L)$, ψ is the polygamma function (or digamma when used with a single parameter), and L is the equivalent number of looks (ENL) of the image.

This Gaussian simplification yields a closed-form estimation and permits fast computation. The approximation can be considered fairly accurate for multilook images such as SWOT high rate (HR) coherent power ($L = 4$) or Sentinel-1 GRD high definition data ($L = 4.4$). Under these hypotheses, the log-reflectivity of the patch under the homogeneous hypothesis H_0 can be estimated as the empirical mean of the log-transformed intensities $\widetilde{I}(k)$ of the patch $I_\square(k)$.

In the following, **1** is a vector of ones with the same dimension as $I(k)$ (the number of pixels in a patch). Under H_0, we use a uniform patch $\widetilde{R}_\mu(k)$ with the Gaussian approximation. Under H1, the estimated patch $\widehat{r}(\widehat{\theta}(k), k)$ is computed from the estimated orientation $\widehat{\theta}(k)$ and profile $\widehat{P}(k, \widehat{\theta}(k))$ under H_1. This way, we get a quadratic expression for the log-transformed GLRT (3). The GLRT boils down to the difference between the reconstruction errors $E_0(k)$ and $E_1(k)$, as presented for one
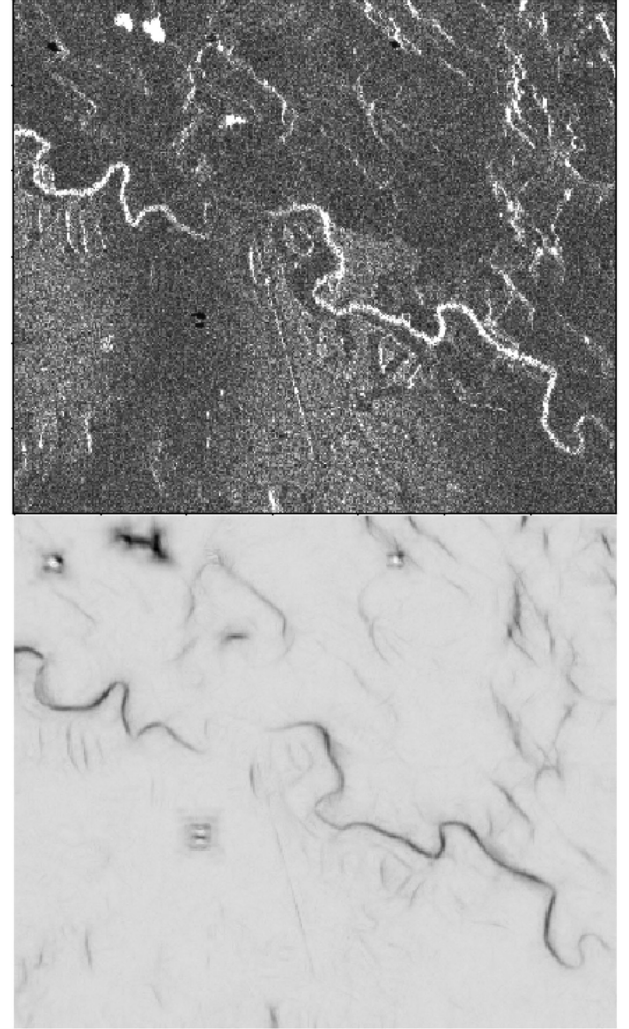

Fig. 5. Simulated SWOT image and linear structure detector response, combining the results for scales 1, 1/2, and 1/3. The response is displayed with inverted gray scale for better visualization.

pixel k in Fig. 4

$$\log(\text{GLRT}(k)) = \frac{1}{2}||\widetilde{I}(k) - \widehat{r}(k)(\widehat{\theta})||^2$$
$$- \frac{1}{2}||\widetilde{I}(k) - \widetilde{R}_\mu(k)||^2$$
$$\log(\text{GLRT}(k)) = E_0(k) - E_1(k). \qquad (3)$$

A more efficient way to compute this GLRT is also presented in [19] and used in our framework. It allows computing the GLRT value at all pixels using Fourier transforms. The detection map can then be improved by combining different scales in a $[S_{\min}, S_{\max}]$ range. This allows for the detection of lines larger than a patch and avoids using large patches that would be computationally expensive. An example of the response of the linear structures detector combining the results for different scales is presented in Fig. 5.
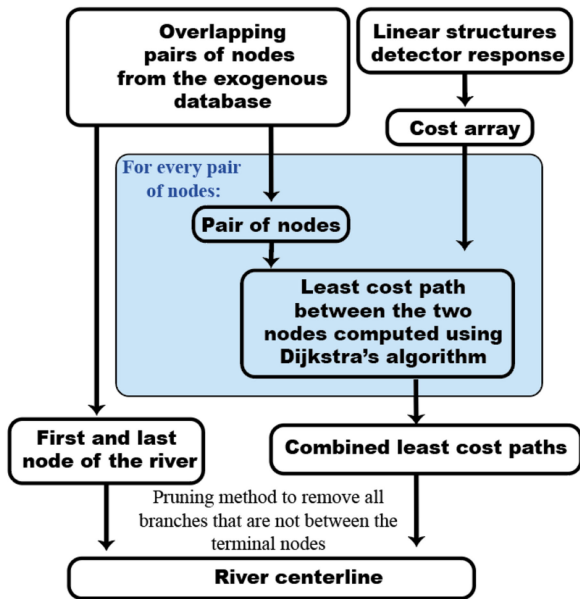
Fig. 6.　Flowchart describing the second step of the algorithm that uses the previously computed linear structures detector response and nodes from the database to compute the river centerline.
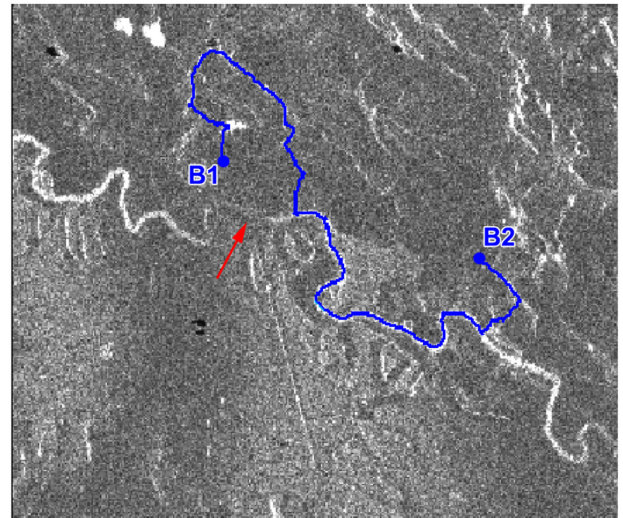

Fig. 7.　Shortest path determination between nodes $B1$ and $B2$ displayed on the original image. The red arrow is pointing to the part of the river that has been missed by the detection. Indeed linear structures that do not correspond to the river caused the centerline to circumvent this part of the river.

C. Accurate Centerline Determination Using Least-Cost Path Algorithm

The second step of the algorithm is to retrieve the actual centerline of the river reach using both the response of the linear structures detector and prior information on the river position. The external database that we use (GRWL) provides for each river reach (about 10-km long) nodes that are 200-m apart along the centerline. From this approximate centerline, at least two approaches can be considered to obtain the actual centerline:

1) to apply an active contour approach such as snake [28] on the entire centerline using the detector response;
2) to consider only some nodes in the centerline and to compute the minimum cost path between pairs of nodes on a cost image derived from the detector response.

A major issue with the snakes approach for this application is its sensitivity to the initialization and to the parameters that determine the evolution of the active contour. A preliminary study showed the difficulty to choose the right parameters and the lack of stability of the results. The proposed method is based on a minimum path between a subset of nodes of the centerlines using Dijkstra's algorithm. A similar method has been proposed by Dillabaugh et al. [15] for optical images, with user-specified start and end points. An overview of this second step of the proposed method is given by Fig. 6 .

We define the cost $C(x, y)$ at every pixel (x, y) based on the line detector response $D(x, y)$ as

$$C(x, y) = [1 - D(x, y)/D_{\max}]^{N_{\text{pow}}} \quad (4)$$

with $D_{\max}$ being the maximum value of the detector response on the whole image and N_{pow} a tuning parameter. N_{pow} adjusts the cost of crossing a pixel whose detector response is not maximal. It has to be high enough to penalize short paths that cut through

a meander but not too high either to prevent the risk of being diverted by a road with a strong line detector response or having numerical computational issues. In the situation where one or both nodes are outside of the river, and provided N_{pow} is high enough, the least-cost path is expected to go from one node to the other through the river via the minimum cost path, as presented in blue between nodes $B1$ and $B2$ in Fig. 7. This approach is robust to situations where the a priori nodes are far away from the actual river (due to changes in the actual river or to projection errors). This has been assessed using nodes with a very exaggerated shift from the true position (over 1 km) in Fig. 7 (and for other Sentinel-1 images in the supplementary materials). We see that the center part of the river segment is correctly detected here, but that close to node B1 an erroneous path has been chosen. This generally occurs in the presence of strong noise or when there are other linear structures in the area.

To cope with this issue and in order to retrieve the entire centerline, we propose to use overlapping pairs of nodes as extremities for the minimum cost path search. Recall that GRWL has a node every 200 m, whereas the pairs of points that we use are in the order of 1–10 km apart. By combining the results for each pair of nodes (for example, the green, blue, and magenta lines in Fig. 8), we obtain the estimated centerline for the whole reach plus one off-river branch between the centerline and every a priori node that does not belong to the actual centerline.

The off-river branches can be easily eliminated using a pruning method. Because of the overlap of the reach nodes, only the pixels on the least-cost path between the end nodes of a reach and the previous reach are kept in the final central line. Fig. 9 shows the result of the pruning of the centerlines in Fig. 8. The final centerline for each river is then stored as a boolean raster C_L of the same size as the image that takes the value 1 on the centerline and 0 elsewhere.
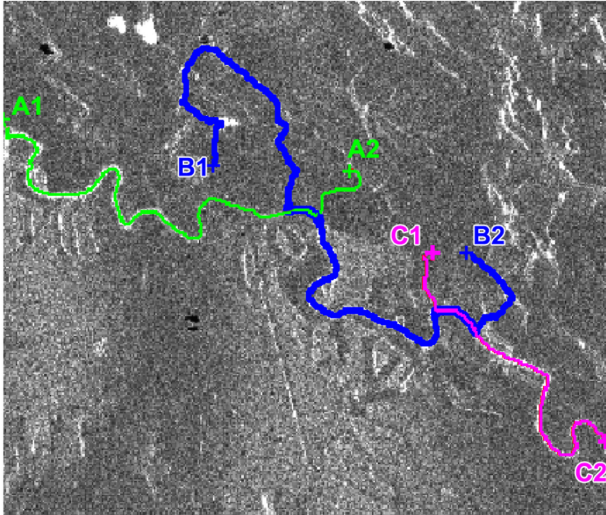
Fig. 8. Visualization on the same image of the result of the least-cost paths for three pairs of nodes: $A1 \rightarrow A2$ in green, $B1 \rightarrow B2$ in blue, and $C1 \rightarrow C2$ in magenta. The centerlines have been widened for better visualization. In this example, the *a priori* nodes have been chosen excessively far from the river to illustrate the robustness of the proposed approach.
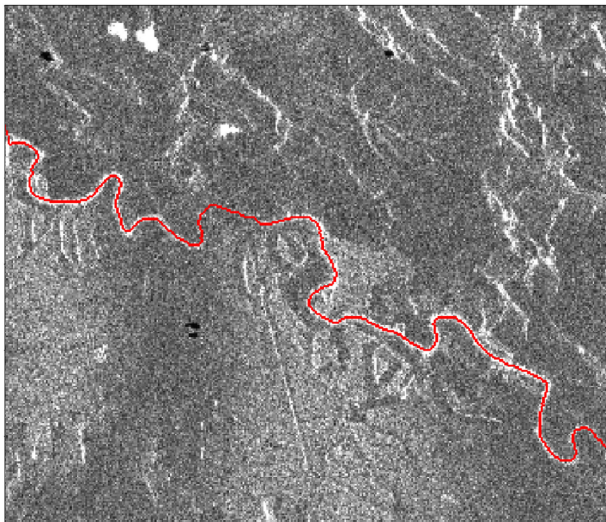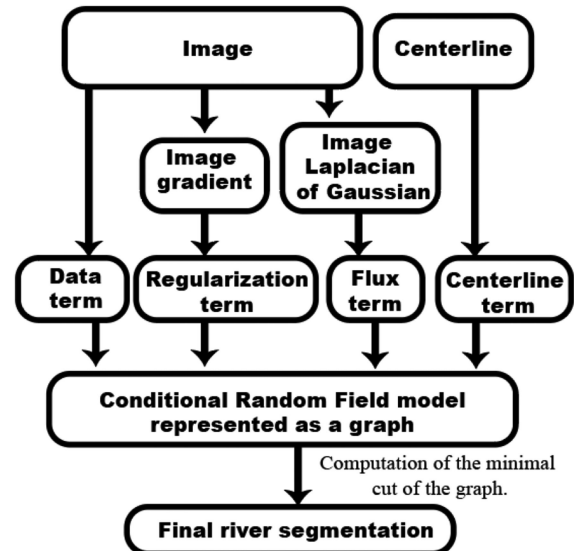

Fig. 10. Flowchart describing the third step of the algorithm that uses the previously computed centerline along with the SAR image to detect the river.

Fig. 9. Centerline obtained after pruning of the previous result. The centerline has been widened for better visualization.

D. Segmentation of the Reach From the Centerline by Conditional Random Field

The last step of the proposed method is to get an accurate segmentation of the river reach using the previously estimated centerline and the SAR image. This can be considered as a region growing problem around the estimated centerline taking into account the intensities in the SAR image. Random walk [29] using the centerline as a seed, morphological approaches or graph-cut approaches [30] with hard constraints could be relevant for this problem, but we did not obtain satisfactory results with these.

Instead, we propose an innovative method based on a CRF [31]. The problem is expressed as the minimization of a global energy function $\mathscr{E}$ that takes both the SAR image and the centerline into account, with an adapted regularization that does not overpenalize narrow rivers. An overview of this method is given by the flowchart in Fig. 10.

The global energy $\mathscr{E}$ which depends on the classification ℓ ($\ell = 1$ for water and $\ell = 0$ for land) is the sum of two data terms, a regularization term, and a flux term

$$\mathscr{E}(\ell, I) = U_{\text{data}}^{I}(\ell, I) + U_{\text{data}}^{C}(\ell, C_L)$$
$$+ U_{\text{reg}}(\ell, I) + U_{\text{flux}}(\ell, I). \quad (5)$$

The two data terms are U_{data}^{I} that ensures fidelity with the image intensity I and U_{data}^{C} that ensures that the centerlines retrieved in the previous step are classified as water. The regularization term U_{reg} is adapted to the segmentation of narrow rivers. Along with this adapted term, we propose a term U_{flux} whose role is to favor a longer water/land contour if this segmentation is in better agreement with the gradients of the SAR image (i.e., to counter-balance the effect of the term U_{reg} that encourages a short contour length).

The image data term U_{data}^{I} is based on a model that considers two likelihoods: a likelihood that depends on the intensity of the image for the water class and a likelihood that is intensity-invariant for the land class. The likelihood for the water class is based on a gamma distribution (6) for the intensity, with two parameters: R_1 for the homogeneous water reflectivity and L for the number of looks. The reflectivity of water R_1 can be estimated using a debiased geometric mean estimator $\widehat{R_1}$ on the intensity I for every pixel belonging to the centerline. In order to increase robustness, the brightest pixels (for Sentinel-1) that can correspond to bridges or boats can be excluded from the computation of the mean. With these variables, the theoretical

distribution of intensity for water is given by

$$\mathrm{p}(I|R_1) = \frac{L^L I^{L-1}}{\Gamma(L) R_1^L} \exp\left(-L \frac{I}{R_1}\right). \qquad (6)$$

The neg-log-likelihood $\mathscr{L}_1$ for the water class ($\ell = 1$) is then

$$\mathscr{L}_1(I|R_1) = K(R_1, L) + \frac{LI}{R_1} + (1 - L) \cdot \log(I) \qquad (7)$$

where $K(R_1, L) = \log(\Gamma(L)) + L \cdot \log(R_1) - L \cdot \log(L)$.

For the land class, in the absence of a model for the distribution of the land class, we consider a uniform likelihood. The constant likelihood value $\mathscr{L}_0$ is chosen so that the data energy of one well-classified pixel (i.e., its neg-log-likelihood) is equal in expectation for both classes

$$\mathscr{L}_0 = K(R_1, L) + L + (L - 1)\left(\log\left(\frac{L}{R_1}\right) - \Psi(L)\right). \qquad (8)$$

Provided that the estimator for water reflectivity $\widehat{R_1}$ is accurate enough, the homogeneous log-likelihood $\mathscr{L}_0 = \mathbb{E}_{I|R_1}[\mathscr{L}_1(I, R_1)]$ (8), with the expected value computed over the water pixels, prevents the classification from being biased toward land.

In order to simplify $\mathscr{L}_1$ and $\mathscr{L}_0$, the constant value $K(R_1, L)$ can be subtracted from both neg-log-likelihoods.

For an elementary surface of the image du centered at u, the image data energy is defined by $U_{\mathrm{data}}^I(du) = \ell(u) \cdot \mathscr{L}_1(I, R_1, L)du + (1 - \ell(u)) \cdot \mathscr{L}_0 du$. Another energy term U_{data}^C ensures that the previously determined centerlines are classified as water. It penalizes by a large value of $K_C \cdot du$ the misclassification as land of any elementary surface du that belongs to a centerline ($C_L(du) = 1$). This energy term is given by $U_{\mathrm{data}}^C(du) = K_C \cdot (1 - \ell(du)) \cdot C_L(du)du$.

Finally, a regularization term ensures that the transitions between water and land are compatible with the gradients of the image by penalizing the transitions that would occur where the gradient magnitude is low or if the boundaries are not orthogonal to the gradient direction.

We want to minimize over the water boundaries the weighted total variation on the label field ℓ that we assume to be continuous and whose spatial gradient at location u is $\|\overrightarrow{\nabla\ell}(u)\|$

$$U_{\mathrm{reg}}(\ell) = \beta \int_{u \in \mathbb{R}^2} w(u) \|\overrightarrow{\nabla\ell}(u)\| du. \qquad (9)$$

The total variation is weighted with

$$w(u) = \exp(-[\overrightarrow{\nabla\ell}(u) \cdot \overrightarrow{\nabla I}(u)]_+ / \lambda). \qquad (10)$$

This weighting w favors localizations of the boundaries that are aligned with the strong gradients of the image. The notation $[x]_+$ returns x if $x > 0$ and 0 otherwise. The variable λ and β are parameters that allow adjusting the regularization and its sensitivity to the gradients.

It can be noted that for sensors with dark rivers on a bright background such as Sentinel-1 or TerraSAR-X, the negative of the gradient $-\overrightarrow{\nabla I}(u)$ should be used instead to segment the rivers.
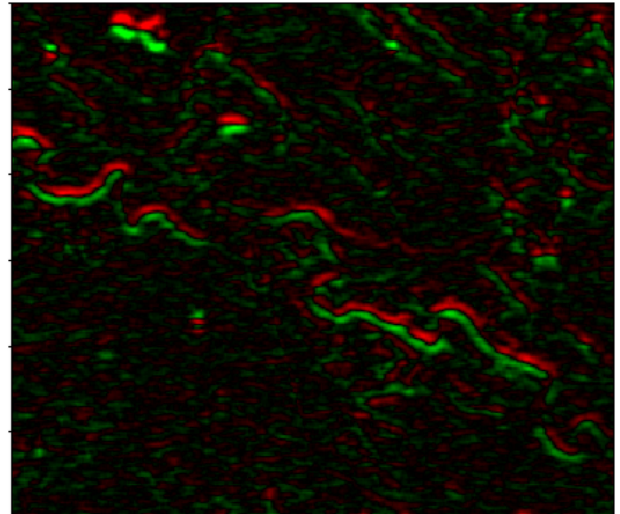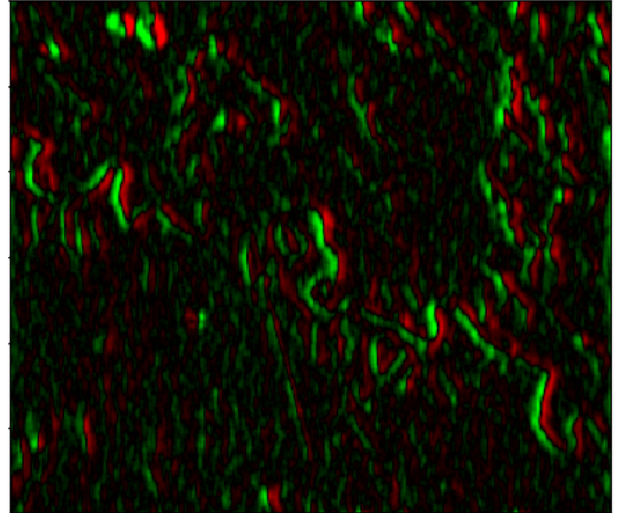

Fig. 11. Gradient for the simulated SWOT image. The positive values are displayed in green, and the negative values are displayed in red. Above: horizontal gradient; below: vertical gradient. The gradients have been computed with the GR approach with a weighting parameter $\alpha = 2.4$ which is a good compromise between smoothing and location for $L = 4$.

To prevent transitions from being encouraged by gradient artifacts caused by speckle noise, we use a gradient adapted to SAR images called gradient by ratio (GR) proposed by Dellinger *et al.* [32], which is an adaptation of ratio of exponentially weighted average proposed by Fjørtoft *et al.* [33]. It computes at each pixel the gradients in the horizontal and vertical directions, as presented in Fig. 11.

The former regularization term U_{reg} can cause excessive regularization especially in low contrast situations and lead to false positives (FPs) and false negatives (FNs) in detection. For example, in SWOT images, a bright sand river inner bank in a meander, also called a point bar (visible in Fig. 12), can be erroneously classified as water. Conversely, in the case of a river with an irregular width, the regularization can lead to an incorrect estimation of the width. To cope with these problems
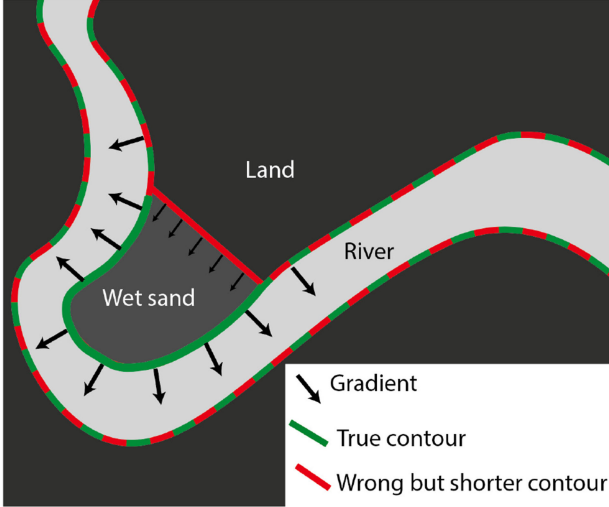
Fig. 12. Illustration of a situation in which using solely the total variation regularization may lead to an erroneous contour detection.
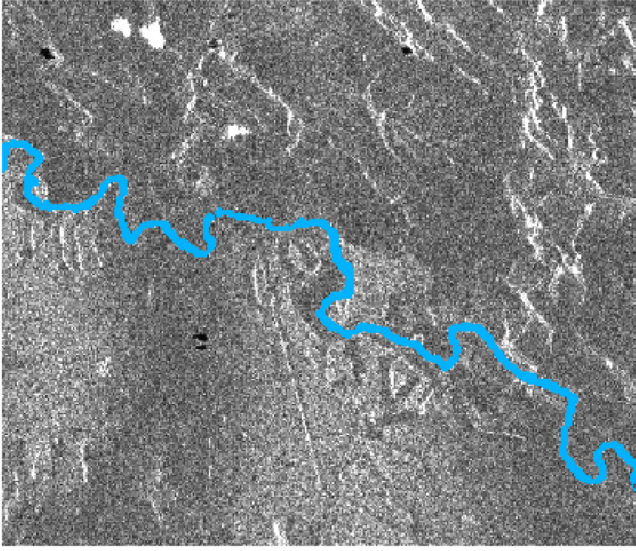

Fig. 13. Result of the CRF segmentation for the same SAR image as in Figs. 5 and 9.

that are caused by the regularization that favors shorter water–land boundaries over longer ones despite the weaker gradient, we introduce an additional term that favors longer boundaries colocated with strong gradients.

The boundaries of the river are expected to be located where the gradient of the SAR image is the strongest within a small neighborhood and to be oriented orthogonally to the gradient. Over the boundary $\partial\{\ell = 1\}$ between land ($\ell = 0$) and water ($\ell = 1$), this criterion locally corresponds to maximizing the dot product between the gradient $\overrightarrow{\nabla}I(u)$ and the unit normal vector of the segmentation naration $\{\ell = 1\}$. Over the whole river, the criterion can be expressed as the outward flux Φ of the gradient through

the boundary $\partial\{\ell = 1\}$

$$
\begin{aligned}
\Phi &= \oint_{u\in\partial\{\ell=1\}} \overrightarrow{\nabla}I(u) \cdot \overrightarrow{n}(u)dl \\
&= \iint_{\{\ell=1\}} \overrightarrow{\nabla} \cdot \overrightarrow{\nabla}I(u)\,\mathrm{d}u
\end{aligned}
\tag{11}
$$

where the second line comes from Ostrogradsky's divergence theorem.

Here, the Laplacian of the image can be approximated with a Laplacian of Gaussian (LoG) operator of parameter σ_L

$$
\overrightarrow{\nabla} \cdot \overrightarrow{\nabla}I \approx \mathrm{LoG}(I, \sigma_L)
\tag{12}
$$

that can be computed using a convolution.

The influence of the flux energy $U_{\text{flux}}(\ell)$ can be balanced with a multiplicative parameter η that adjusts its effect

$$
U_{\text{flux}}(\ell) = \int_{u\in\mathbb{R}^2,\ell(u)=1} \eta\cdot\mathrm{LoG}(I, \sigma_L)du.
\tag{13}
$$

The sign of η depends on the sensor: $\eta < 0$ for SWOT (water generally brighter than land) and $\eta > 0$ for Sentinel-1 (land mostly brighter than water).

By combining the four terms, U_{data}^I, U_{data}^C, U_{reg}, U_{flux} of $\mathscr{E}$, we can write the segmentation problem as a minimization problem

$$
\begin{aligned}
\arg\min_{\ell} &\int_{u\in\mathbb{R}^2,\ell(u)=1} \mathscr{L}_1(I, R_1, L) + \eta \cdot \mathrm{LoG}(I, \sigma_L)du \\
&+ \int_{u\in\mathbb{R}^2,\ell(u)=0} \mathscr{L}_0 + C_L(u) \cdot K_C du \\
&+ \beta \int_{u\in\mathbb{R}^2} w(u)\|\overrightarrow{\nabla\ell}(u)\|du.
\end{aligned}
\tag{14}
$$

This equation can be discretized as

$$
\begin{aligned}
\arg\min_{l} &\sum_i \ell(i)(\mathscr{L}_1(I, R_1, L) + \eta \cdot \mathrm{LoG}(I, \sigma)) \\
&+ (1 - \ell(i))(\mathscr{L}_0 + C_L(i)) \\
&+ \beta \sum_{i\sim j} w(i, j) \cdot |\ell(j) - \ell(i)|
\end{aligned}
\tag{15}
$$

with $w(i, j) = \exp(-[(\ell(j) - \ell(i))(I(j) - I(i))]_+/\lambda)$, where $i \sim j$ means that j is an 8-neighbor of i. In the case of pixels that are 8-neighbors of i but not 4-neighbors, λ is multiplied by $\sqrt{2}$.

The minimization problem presented in (15) can be solved using a minimal cut approach such as the one proposed by Boykov *et al.* [30], with asymmetric edges on a directed graph. An example of result is presented in Fig. 13.

III. EXPERIMENTAL RESULTS

In this section, we evaluate the interest and characterize the performances of our method in segmenting small rivers in SAR images using a prior database, both for SWOT and Sentinel-1 images. Even if the images from the experimental dataset have been chosen to be as representative as possible of various situations, the comprehensive calibration of the algorithm on a specific sensor is beyond the scope of our experiments.

TABLE I
SENTINEL-1 GRD IMAGES USED FOR OUR EXPERIMENTS

Image #-name	River name	Location	Date	Polarization	River width	Size (pixels)
1 - Des Moines	Racoon	Des Moines, Iowa, USA	2018-08-02	VH	40m - 120m	1313×1750
2 - Sunar	Sunar	Garhakota, Madhya Pradesh, India	2018-06-22	VH	40m - 150m	1026 × 923
3 - Gaoual	Tomine Koumba	Near Gaoual, Guinea	2018-07-15	VH	30m - 130m 30m - 130m	927×1854
4 - Angers	Maine Loire Louet anabranch	Angers, Pays de la Loire, France	2019-12-02	VV	100m - 150m 200m - 1000m 25m-120m	927×1854
5 - Garonne	Garonne	North of Toulouse, France	2020-02-09	VV	80m - 200m	1109×1704
6 - Redon	Oust Vilaine	Redon, Brittany France	2018-07-04	VH	15m - 60m 40m - 160m	618×773
7 - Régina	Arataï Approuague	Régina, French Guiana, France	2017-10-11	VH	25m - 100m 100m - 150m	553×1216

The results presented below have been obtained using our published code[1] that uses the PyMaxFlow[2] wrapper to Vladimir Kolmogorov's graph cut solver presented in [34].

A. Dataset

Our method has been tested on Sentinel-1 GRD images and on simulated SWOT HR images.

1) Sentinel-1: We used Sentinel-1 GRD images (more specifically, interferometric wide GRD high definition images) in VV or VH polarization that have been downloaded from a Copernicus Open-Access mirror and cropped around the study area without orthorectification or calibration.

These images have been multilooked by a factor of five in the range direction from the single look complex images and have an ENL of about 4.4. Their spatial resolution is about 20.5m az × 22.m rg and each pixel corresponds to a 10m × 10m square on the ground.

We use seven images in our Sentinel-1 dataset, presented in Table I, corresponding to various examples of small rivers with different kinds of environments.

These images are associated with a ground truth that has been manually drawn on the SAR image using GIMP software, with the help of Open Street Map and optical images provided by Bing displayed over the SAR images with QGIS software to help distinguish between actual rivers and other dark linear structures. This ground truth is not binary but classifies the pixels of the images into three classes: Land, Water, and Uncertain classification. The Uncertain class corresponds to pixels for which it was not possible to determine whether or not it should belong to the river. We used it for our ground truth in the following four situations:

1) isolated strong reflectors in rivers (most likely boats);
2) bridges over rivers;
3) small anabranches (diverging branches of a river, separated by an island, that re-enter the main stream downstream);
4) flooded areas or small lakes that are only partially connected to a river.

All Sentinel-1 image extracts and associated ground truth are made available in the same repository as our published code.

2) SWOT: Concerning SWOT images, as the SWOT satellite has not yet been launched, all test images have been simulated with the jet propulsion laboratory HR science simulator [35]. The simulation is based on high-resolution DEMs and landcover maps, near-nadir Ka-band normalized backscattering coefficient functions for water and various landcover classes, and actual instrument characteristics. It accounts for speckle, geometric effects such as layover, and azimuth smearing due to the limited coherence time of water. These images are associated with the water mask that has been used for the simulation as ground truth.

We used three simulated images for our experiments. All images have been simulated considering pessimistic assumptions about the performances of the sensor (worst-case scenario). The first image has been simulated from Lidar and high-resolution landcover data on the Saline River, Lincoln County, KS, USA and presented in the previous part. This image has been simulated with the so-called dark water phenomenon. Dark water is water with a very low contrast compared to land and is caused by very low water surface roughness at low wind speed. This dark water phenomenon, and numerous bright land structures, make river detection especially difficult on this image. The two other images have been simulated using Lidar data on the Rhnône delta, France. Unlike the Saline River image, these two images have been simulated without dark water: The contrast between water and land is more homogeneous. Image 9 corresponds to the downstream Petit-Rhnône river, whereas image 10 corresponds to the upstream Petit Rhône river with two small channels.

The SWOT images are summarized in Table II. The river widths are given in pixels here and not in meters as the pixel ground range spacing in SWOT depends on the position in the swath.

B. Metrics

In order to quantitatively assess the performance of the water detection compared to our ground truth, we use the same six metrics as Lobry *et al.* [7]. These metrics are based on the number of pixels considered as true positives (TPs) for adequately classified water, true negatives (TNs) for adequately classified land, FNs for water classified as land, and FPs for land classified

TABLE II
SIMULATED SWOT IMAGES USED FOR OUR EXPERIMENTS

Image # - name	River name	Location	Hypothesis on sensor performances	Simulated dark water	River width (pixels)	Size (pixels)
8 - Saline	Saline	Lincoln County, Kansas, USA	Worst Case	Yes	2-5	301×351
9 - Petit Rhône downstream	Petit Rhône	Camargue France	Worst Case	No	3-14	700×800
10 - Petit Rhône Upstream and channels	Petit Rhône Chanel Bas-Rhône Languedoc Channel of Rhône in Sète	Camargue France	Worst Case	No	2-8	800×730

TABLE III
PARAMETERS USED FOR THE EXPERIMENTS

	Line detection			Centerline detection	River segmentation			
	Patch size N	Scale Range $[S_{min}, S_{max}]$	Angular step θ_{step}	Linear detector power N_{pow}	Regularization β	λ	Flux σ_L	η
SWOT	9	[1,3]	3°	70	4	0.2	3	6
Sentinel-1 GRD	9	[1,4]	3°	10	15	0.2	3	6

as water

$$\text{Recall} = \frac{\text{TP}}{\text{TP} + \text{FN}} \qquad (16)$$

$$\text{FPR} = \frac{\text{FP}}{\text{FP} + \text{TN}} \qquad (17)$$

$$\text{Precision} = \frac{\text{TP}}{\text{TP} + \text{FP}} \qquad (18)$$

$$F\text{-score} = 2\frac{\text{Precision} \times \text{Recall}}{\text{Precision} + \text{Recall}} \qquad (19)$$

$$\text{ER} = \frac{\text{FP} + \text{FN}}{\text{TP} + \text{FN}} \qquad (20)$$

$$\text{MCC} = \frac{\text{TP} \times \text{TN} - \text{FP} \times \text{FN}}{\sqrt{(\text{TP} + \text{FN})(\text{FP} + \text{TN})(\text{TP} + \text{FP})(\text{TN} + \text{FN})}}. \qquad (21)$$

The recall is the proportion of actual water pixels that are classified as water. The FPR is the proportion of land pixels that are classified as water. The precision is the proportion of actual water among all the pixels classified as water. The *F*-score is the harmonic mean of precision and recall and will be our main metrics. ER is the ratio between the number of incorrectly classified pixels and the number of actual water pixels. This metric is similar to the metric of the SWOT mission science requirements [36] but computed in radar geometry instead of ground geometry. The Matthews correlation coefficient (MCC) [37] is another metric that takes into account the over-representation of land in the context of river detection.

C. Implementation

For each image, we extract the rivers using our method by choosing a very limited number of prior centerline nodes in order to highlight the robustness of the proposed approach. For single rivers (except for image 8, used as an example in the previous part), we use only two nodes: one for each endpoint. When two rivers are joining in a confluence, we locate one node on the confluence and one node at each endpoint of the two upstream

rivers and of the downstream river. In the case of an anabranch (e.g., in Angers image), a node is added in the anabranch in order to prevent its centerline from going through the main stream. The nodes that have been used are plotted on the images.

We used the parameters presented in Table III. These parameters have been chosen empirically by testing multiple values on the SWOT simulated image Saline. We manually increased the maximum scale $S_{\max}$ of the detection of the linear structures from 3 to 4 to account for the wider range of river width in our use of Sentinel-1 images and decreased the N_{pow} parameter from 70 to 10 in order to be more robust to dark roads. For both kinds of images, we used $L = 4$ for our experiments.

The results could have been improved by fitting the parameters to the type of image (SWOT, Sentinel-1 VV, and Sentinel-1 VH) or even to the environment (urban area, rain-forest, desert, etc.), but our main goal for these experiments was to show satisfactory performances without fine-tuning of the parameters.

Concerning the optimization of the code we use, we improved the computation of the linear features detection, which is by far the slowest step, by using the fast computational approach proposed in [19]. Moreover, the convolutions are processed in the Fourier domain and the FFT of the image is computed only once for all the orientations. However, the computing speed could still be dramatically improved by using parallel processing.

D. Results

Table IV gives the metrics for each image in our dataset. The metrics are computed only for river detection (the detection of surrounding lakes is considered to be a separate task, already addressed by [7]). Three images are presented in detail below, with their associated detection maps: Image 1 (Des Moines) is representative of the results obtained with our method for typical Sentinel-1 images in urban areas, image 2 (Sunar) to present an example where the centerline detection is not successful, and image 9 (Petit-Rhnône Downstream) as an example for SWOT images. All ten images of our dataset and the corresponding segmentation results are presented in the supplementary materials,

TABLE IV
SUMMARY OF THE METRICS FOR EACH RESULT

| Number	Name (sensor)	Method	Precision (%)	Recall (%)	FPR (%)	**F-Score (%)**	ER (%)	MCC (%)	Execution time (s)
1	Des Moines (S1)	Proposed	92.44	93.35	0.13	**92.89**	14.29	92.78	57.73s
2	Sunar (S1)	Proposed	82.36	81.71	0.15	**82.03**	35.79	81.88	89.32s
3	Gaoual (S1)	Proposed	92.51	89.09	0.12	**90.77**	18.12	90.64	212.96s
4	Angers (S1)	Proposed	98.90	94.04	0.05	**96.40**	7.01	96.28	160.96s
5	Garonne (S1)	Proposed	97.60	82.44	0.02	**89.38**	19.59	89.60	166.01s
6	Redon (S1)	Proposed	90.28	92.70	0.15	**91.47**	17.28	91.35	47.48s
7	Régina (S1)	Proposed	89.33	82.95	0.18	**86.02**	26.96	85.83	62.86s
8	Saline (SWOT)	Proposed	63.24	94.45	1.02	**75.76**	60.45	76.81	10.45s
		Baseline	5.30	87.58	33.87	**10.00**	1576.64	65.92	/
9	Petit Rhône downstream (SWOT)	Proposed	80.71	89.46	0.57	**84.86**	31.92	84.56	47.23s
		Baseline	91.00	9.80	0.03	**17.69**	91.17	9.66	/
10	Petit Rhône upstream and channels (SWOT)	Proposed	73.07	87.45	0.58	**79.62**	44.78	79.55	57.17s
		Baseline	87.32	8.89	0.02	**16.14**	92.40	8.80	/
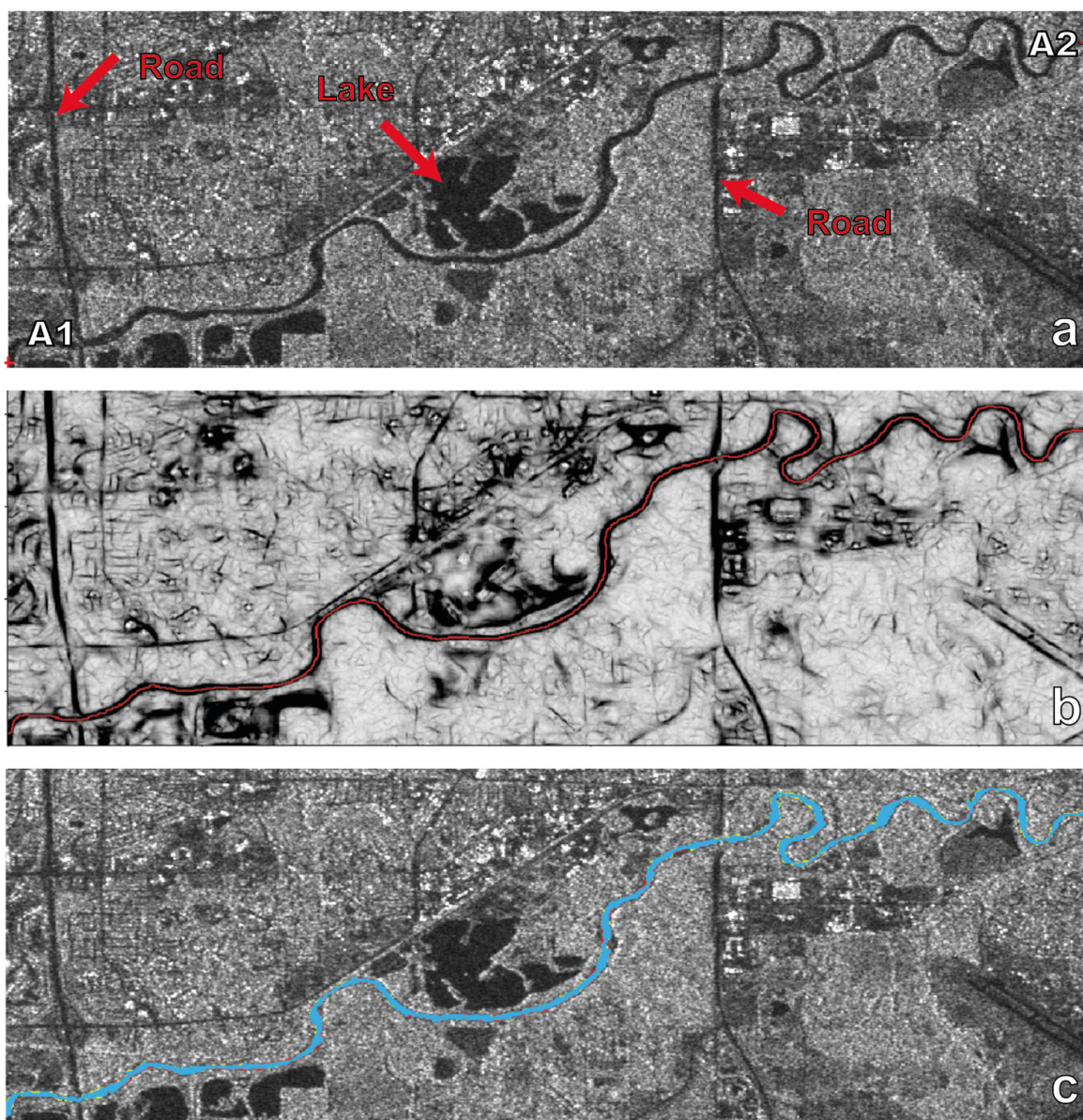
Fig. 14. Image 1 (Des Moines): (a) SAR image with annotations, (b) centerline (in red) on the linear features detector, and (c) final segmentation. A1 and A2 mark the two nodes used as prior information. The color map of the line detector has been inverted and the centerline has been widened for better visualization. In (c), the true positives are displayed in blue, the false positives in yellow, and the false negatives in red. True negatives are displayed as the actual SAR image pixels.
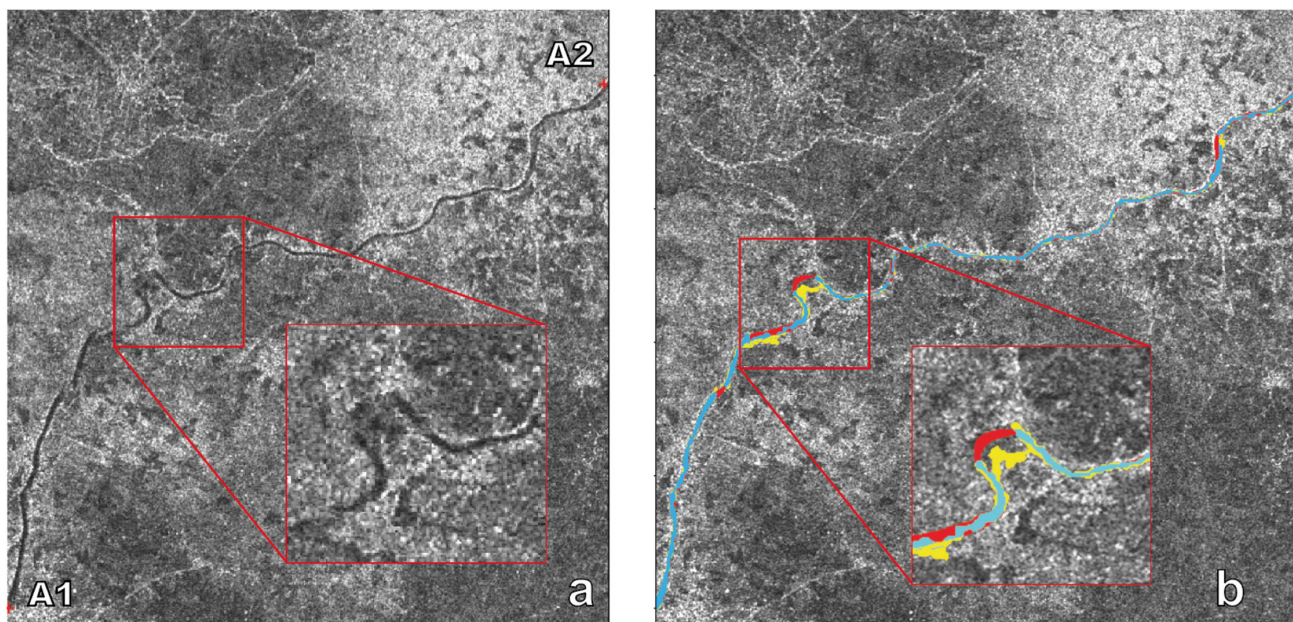
Fig. 15. Image 2 (Sunar): (a) SAR image with annotations and (b) final segmentation. A1 and A2 mark the two nodes used as prior information. The closeup squared in red in both images show a meander in which the segmentation is unsuccessful as the centerline bypasses the meander. A1 and A2 mark the two nodes used as prior information. In (b), the true positives are displayed in blue, the false positives in yellow, and the false negatives in red. True negatives are displayed as the actual SAR image pixels.
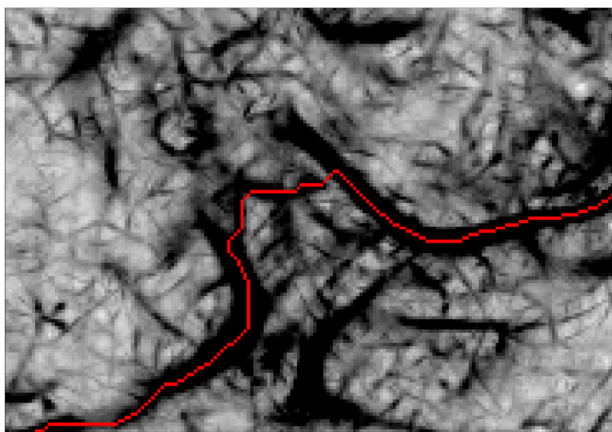

Fig. 16. Image 2 (Sunar): Zoom on the red square area in Fig. 15, with the response of the linear structure detector (inverted gray scale) and the detected centerline (red, widened for better visualization).

and for Sentinel-1 images, the results can be reproduced using our published code.

Example 1: Image 1 (Des Moines), displayed in Fig. 14 , shows that our method leads to correct detection of the whole river, despite using only two nodes as prior information and although the river is meandering. The centerline (b) has been correctly classified with the proposed approach based on the response of the linear feature detector. The segmentation of the river from the centerline using our CRF approach also gives good results in this example. The river contour is relatively well respected. It can be noted that, despite a reflectivity similar to the reflectivity of the river, the lake (which is not connected to the

river) and two large roads [Fig. 14(a)] are not misclassified as rivers. Our approach avoids two typical pitfalls of river detection on SAR images that are lakes close to rivers and highways.

Example 2: Image 2 (Sunar) presented in Fig. 15 illustrates a possible issue with the proposed approach when using insufficient exogenous information about the location of the river. If a dark linear structure in a river meander in a Sentinel-1 image creates a shorter path between two a priori nodes of the centerline and if the actual river is not identifiable, the detected centerline will be incorrect. This leads to FPs on the dark linear structure and FNs in the part of the river that has been bypassed, such as in Fig. 16 . The resulting classification is erroneous for this part of the river. However, this does not significantly affect the classification of the remainder of the river, as the estimation of the parameters is robust enough.

A possible improvement would be to use more centerline nodes as exogenous information and to use a postprocessing step to flag as uncertain the river parts where the reflectivity is too high (possibly sand, mud, or flooded vegetation) and remove them if appropriate.

Example 3: Image 9 (Petit Rhône downstream), presented in Fig. 17 , illustrates the behavior of the proposed method applied to simulated SWOT HR images. In this example, the river centerline has been correctly detected and the river segmentation is relatively accurate except for some FPs caused by speckle noise, and a very small connected channel that has not been detected. In comparison with the baseline method [7] that only detects a small part of the narrow river, the proposed approach shows an improved detection. Because our approach does not detect other water surfaces, but only rivers that would have been missed by the generic method, both approaches are complementary.
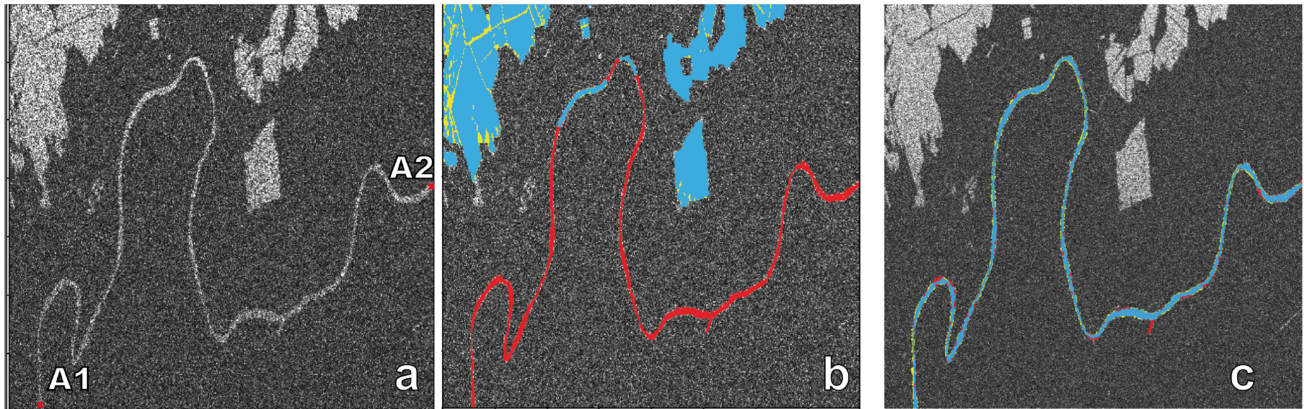
Fig. 17.   Image 9 (Petit-Rhnône downstream): (a) SAR image with *a priori* nodes, (b) segmentation with the baseline MRF method, and (c) proposed method segmentation. A1 and A2 mark the two nodes used as prior information. In (b) and (c), the true positives are displayed in blue, the false positives in yellow, and the false negatives in red. True negatives are displayed as the actual SAR image pixels.

It can be noted that for SWOT images, the bright area corresponding to the river response might be slightly larger than the river itself in the azimuth direction because water is moving and does not necessarily remain coherent during the entire SAR integration time. This issue could be addressed by a morphological postprocessing in order to erase such FP pixels and thereby improve the precision.

IV. CONCLUSION

In this article, an innovative river extraction method is proposed and evaluated. The originality of our approach is that it uses an exogenous river database in order to guide the river detection. The proposed technique consists of three phases: First, computing the response of a linear feature detector, then detecting the centerline using the response and the prior river nodes, and, finally, segmenting the river around the previously detected centerline using a CRF approach. Experiments performed on both Sentinel-1 and simulated SWOT HR images have shown that our method performs well including in low contrast situations and for very narrow rivers of only a few pixels.

The proposed method has been developed in the context of the SWOT mission to process SWOT HR images that are single-polarization and cannot easily be combined with images from other sensors. This leads us to design a resilient method for river segmentation in such images. While the proposed method achieves good results in detecting rivers in single-polarization (VV or VH) Sentinel 1 images, these results might be further improved by using jointly the two polarizations or even by merging information from optical images when available. The two polarizations of Sentinel-1 images could be combined by simply multiplying pixelwise the VV and VH amplitude images as it has been proposed by Nunziata *et al.* [38] for coastal line segmentation or as used in Ferrentino *et al.* [39] for segmenting a lake. This would require a minor adaptation of the last step of the proposed method (as the product is not Gamma-distributed) but could improve the discrimination between dark river banks and water. Another possible adaptation of our method concerns the first step of linear structure detection. Indeed, while our

approach gives good results, a limitation is that it is quite time-consuming. Even if this could be significantly improved with a more optimized implementation of our approach, a faster deep learning based linear structure detector for SAR images could potentially replace the current first step in the future.

The direct application of the proposed framework has obvious potential for monitoring rivers included in the GRWL database, but it may also be adapted to the detection of rivers unknown to the database. For example, if other hydrological information or a DEM indicates that a small tributary is missing from the database, our approach can help to retrieve it by using two inputs: one node in the main river and one node placed further up in the expected tributary.

Other interesting research tracks concern the adaptation of the proposed approach to other applications than river monitoring, for example, road extraction in SAR images.

REFERENCES

[1] J.-F. Pekel, A. Cottam, N. Gorelick, and A. S. Belward, "High-resolution mapping of global surface water and its long-term changes," *Nature*, vol. 540, no. 7633, pp. 418–422, Dec. 2016.

[2] G. H. Allen and T. M. Pavelsky, "Global extent of rivers and streams," *Science*, vol. 361, no. 6402, pp. 585–588, 2018.

[3] M. Durand, L. Fu, D. P. Lettenmaier, D. E. Alsdorf, E. Rodriguez, and D. Esteban-Fernandez, "The surface water and ocean topography mission: Observing terrestrial surface water and oceanic submesoscale eddies," *Proc. IEEE*, vol. 98, no. 5, pp. 766–779, May 2010.

[4] C. Huang, Y. Chen, S. Zhang, and J. Wu, "Detecting, extracting, and monitoring surface water from space using optical sensors: A review," *Rev. Geophys.*, vol. 56, no. 2, pp. 333–360, 2018.

[5] H. Liu and K. C. Jezek, "Automated extraction of coastline from satellite imagery by integrating canny edge detection and locally adaptive thresholding methods," *Int. J. Remote Sens.*, vol. 25, no. 5, pp. 937–958, 2004.

[6] C. Cazals *et al.*, "Mapping and characterization of hydrological dynamics in a coastal marsh using high temporal resolution sentinel-1a images," *Remote Sens.*, vol. 8, no. 7, Jul. 2016. Art. no. 570.

[7] S. Lobry, L. Denis, B. Williams, R. Fjørtoft, and F. Tupin, "Water detection in SWOT HR images based on multiple Markov random fields," *IEEE J. Sel. Topics Appl. Earth Observ. Remote Sens.*, vol. 12, no. 11, pp. 4315–4326, Nov. 2019.

[8] M. Silveira and S. Heleno, "Separation between water and land in SAR images using region-based level sets," *IEEE Geosci. Remote Sens. Lett.*, vol. 6, no. 3, pp. 471–475, Jul. 2009.

[9] F. Cao, F. Tupin, J. Nicolas, R. Fjørtoft, and N. Pourthié, "Extraction of water surfaces in simulated ka-band SAR images of KaRIn on SWOT," in *Proc. IEEE Int. Geosci. Remote Sens. Symp.*, 2011, pp. 3562–3565.

[10] S. Valero, J. Chanussot, J. Benediktsson, H. Talbot, and B. Waske, "Advanced directional mathematical morphology for the detection of the road network in very high resolution remote sensing images," *Pattern Recognit. Lett.*, vol. 31, no. 10, pp. 1120–1127, 2010,

[11] S. Klemenjak, B. Waske, S. Valero, and J. Chanussot, "Automatic detection of rivers in high-resolution SAR data," *IEEE J. Sel. Topics Appl. Earth Observ. Remote Sens.*, vol. 5, no. 5, pp. 1364–1372, Oct. 2012.

[12] M. O. Sghaier, S. Foucher, and R. Lepage, "River extraction from high-resolution SAR images combining a structural feature set and mathematical morphology," *IEEE J. Sel. Topics Appl. Earth Observ. Remote Sens.*, vol. 10, no. 3, pp. 1025–1038, Mar. 2017.

[13] B. Han and Y. Wu, "River extraction of SAR images via active contours driven by adaptive global fitting energies," *Int. J. Remote Sens.*, vol. 39, no. 20, pp. 6995–7013, 2018.

[14] A. Gruen and H. Li, "Semiautomatic road extraction by dynamic programming," in *ISPRS Commission III Symposium: Spatial Information from Digital Photogrammetry and Computer Vision*, vol. 2357, H. Ebner, C. Heipke, and K. Eder, Eds., Bellingham, WA, USA: SPIE, 1994, pp. 324–332.

[15] C. R. Dillabaugh, K. O. Niemann, and D. E. Richardson, "Semi-automated extraction of rivers from digital imagery," *GeoInformatica*, vol. 6, no. 3, pp. 263–284, 2002.

[16] T. Coulthard and M. Van De Wiel, "Modelling river history and evolution," *Philos. Trans. Roy. Soc. A: Math., Phys. Eng. Sci.*, vol. 370, no. 1966, pp. 2123–2142, May 2012.

[17] J. Hooke, "Changes in river meanders: A review of techniques and results of analyses," *Prog. Phys. Geogr.: Earth Environ.*, vol. 8, no. 4, pp. 473–508, 1984.

[18] E. W. Dijkstra, "A note on two problems in connexion with graphs," *Numerische Math.*, vol. 1, no. 1, pp. 269–271, 1959.

[19] N. Gasnier, L. Denis, and F. Tupin, "Generalized likelihood ratio tests for linear structure detection in SAR images," in *Proc. EUSAR 2021; 13th Eur. Conf. Synthetic Aperture Radar, to be published*, 2021, in press.

[20] D. Geman and B. Jedynak, "An active testing model for tracking roads in satellite images," *IEEE Trans. Pattern Anal. Mach. Intell.*, vol. 18, no. 1, pp. 1–14, Jan. 1996.

[21] M. A. Fischler, J. M. Tenenbaum, and H. C. Wolf, "Detection of roads and linear structures in low-resolution aerial imagery using a multisource knowledge integration technique," in *Readings in Computer Vision*. Amsterdam, The Netherlands: Elsevier, 1987, pp. 741–752.

[22] F. Deschênes and D. Ziou, "Detection of line junctions and line terminations using curvilinear features," *Pattern Recognit. Lett.*, vol. 21, no. 6, pp. 637–649, 2000.

[23] G. J. Vanderbrug, "Line detection in satellite imagery," *IEEE Trans. Geosci. Electron.*, vol. 14, no. 1, pp. 37–44, Jan. 1976.

[24] S. Movaghati, A. Moghaddamjoo, and A. Tavakoli, "Road extraction from satellite images using particle filtering and extended Kalman filtering," *IEEE Trans. Geosci. Remote Sens.*, vol. 48, no. 7, pp. 2807–2817, Jul. 2010.

[25] O. Hellwich, I. Laptev, and H. Mayer, "Extraction of linear objects from interferometric SAR data," *Int. J. Remote Sens.*, vol. 23, no. 3, pp. 461–475, 2002.

[26] F. Tupin, H. Maitre, J. F. Mangin, J. M. Nicolas, and E. Pechersky, "Detection of linear features in SAR images: Application to road network extraction," *IEEE Trans. Geosci. Remote Sens.*, vol. 36, no. 2, pp. 434–453, Mar. 1998.

[27] H. Xie, L. E.Pierce, and F. T. Ulaby, "Statistical properties of logarithmically transformed speckle," *IEEE Trans. Geosci. Remote Sens.*, vol. 40, no. 3, pp. 721–727, Mar. 2002.

[28] M. Kass, A. Witkin, and D. Terzopoulos, "Snakes: Active contour models," *Int. J. Comput. Vis.*, vol. 1, no. 4, pp. 321–331, 1988.

[29] L. Grady, "Random walks for image segmentation," *IEEE Trans. Pattern Anal. Mach. Intell.*, vol. 28, no. 11, pp. 1768–1783, Nov. 2006.

[30] Y. Y. Boykov and M. Jolly, "Interactive graph cuts for optimal boundary region segmentation of objects in N-D images," in *Proc. 8h IEEE Int. Conf. Comput. Vis.*, vol. 1, 2001, pp. 105–112.

[31] J. D. Lafferty, A. McCallum, and F. C. N. Pereira, "Conditional random fields: Probabilistic models for segmenting and labeling sequence data," in *Proc. 18th Int. Conf. Mach. Learn., Ser.*, San Francisco, CA, USA: Morgan Kaufmann Publishers Inc., 2001, pp. 282–289.

[32] F. Dellinger, J. Delon, Y. Gousseau, J. Michel, and F. Tupin, "SAR-SIFT: A SIFT-Like algorithm for SAR images," *IEEE Trans. Geosci. Remote Sens.*, vol. 53, no. 1, pp. 453–466, Jan. 2015.

[33] R. Fjørtoft, A. Lopes, P. Marthon, and E. Cubero-Castan, "An optimal multiedge detector for SAR image segmentation," *IEEE Trans. Geosci. Remote Sens.*, vol. 36, no. 3, pp. 793–802, May 1998.

[34] Y. Boykov and V. Kolmogorov, "An experimental comparison of min-cut/max- flow algorithms for energy minimization in vision," *IEEE Trans. Pattern Anal. Mach. Intell.*, vol. 26, no. 9, pp. 1124–1137, Sep. 2004.

[35] E. Peral *et al.*, "SWOT Simulator Quick User Guide," JPL/Caltech, CA, USA, Tech. Rep. D-79123, 2014.

[36] E. Rodríguez, "Science requirements document, revision B," JPL/Caltech, CA, USA, Tech. Rep. D-61923, 2018.

[37] B. Matthews, "Comparison of the predicted and observed secondary structure of t4 phage lysozyme," *Biochimica et Biophysica Acta (BBA) - Protein Struct.*, vol. 405, no. 2, pp. 442–451, 1975.

[38] F. Nunziata, A. Buono, M. Migliaccio, and G. Benassai, "Dual-polarimetric C- and X-band SAR data for coastline extraction," *IEEE J. Sel. Topics Appl. Earth Observ. Remote Sens.*, vol. 9, no. 11, pp. 4921–4928, Nov. 2016.

[39] E. Ferrentino, F. Nunziata, A. Buono, A. Urciuoli, and M. Migliaccio, "Multipolarization time series of sentinel-1 SAR imagery to analyze variations of reservoirs' water body," *IEEE J. Sel. Topics Appl. Earth Observ. Remote Sens.*, vol. 13, pp. 840–846, 2020.

Nicolas Gasnier (Student Member, IEEE) graduated in electrical engineering from École Normale Supérieure de Cachan, Cachan, France, in 2018, and received the M.Sc. degree in computer science (*summa cum laude*) from Sorbonne Université, Paris, France in 2018 in 2018. He is currently working toward the Ph.D. degree in signal, images, automatics, and robotics with Télécom Paris, Institut Polytechnique de Paris, Palaiseau, France, and the French Space Agency, Centre National d'Etudes Spatiales (CNES), Toulouse, France, and CS GROUP - France, Toulouse, France.

Loïc Denis received the M.Sc. degree in electrical engineering from the CPE Lyon, France, in 2003, the Ph.D. degree in 2006 and Habilitation degree in 2018 both in imaging science from the Universit Jean Monnet, Saint-Etienne, France.

He is currently the Associate Professor with the Université Jean Monnet, Saint-Etienne, France. His research interests include image denoising and reconstruction, robust signal processing, source detection, and machine learning with applications in remote sensing, diffractive microscopy, and astronomy.

Dr. Denis is a corecipient of IEEE ICIP Best Student Paper Award (2010), EURASIP EUSIPCO Best Student Paper Award (2015), and the IEEE Geoscience and Remote Sensing Society 2016 Transactions Prize Paper Award (2016).

Roger Fjørtoft (Member, IEEE) received the M.S. degree in electronics from the Norwegian Institute of Technology, Trondheim, Norway, in 1993, and the Ph.D. degree in signal processing, image processing, and communications from Institut National Polytechnique, Toulouse, France, in 1999.

He was a Senior Research Scientist with Norwegian Computing Center, Oslo, Norway, from 2000 to 2003, and since then, he has been with the French Space Agency, Centre National d'Etudes Spatiales (CNES), Toulouse, France. He is currently with the Radar Algorithms, Processing and Products Department (DSO/SI/TR), where he leads the development of algorithms for the operational processing of high-resolution data from the upcoming SWOT mission, prepared jointly by NASA/JPL, and CNES.

Frédéric Liège was born in Aubagne, France, on January 1, 1968. He received the Ph.D. degree in geography and remote sensing from the University of Paris IV-Sorbonne, Paris, France, and the Military Technical Certificate in engineering sciences from the Military Scientific and Technical High School in 1997.

He was an Associate Researcher with the UMR8185 CNRS/ENS/EHSS Image Processing Lab, National Center for Scientific Research, Paris, France, from 1997 to 2005. In parallel, he was an image processing expert in the French MoD, involved in advanced sensor and image processing studies and major military/dual-use multinational spatial programs in the fields of visible, infrared, radar, and hyperspectral sensors. From 1997 to 2008, he took part in most of major technical and prospective studies of French MoD in hyperspectral, infrared, and radar domain and user ground segments designs and implementation. In this context, he was the Cofounder and Cochairman of the French MoD hyperspectral workgroup and member of the Infrared and Radar MoD workgroups for operational requirements purpose. He was also the representative of the French General Staff in the CNES Hyperspectral Group which published National Hyperspectral Synthesis Report in 2008 and in the SET-ET-054 hyperspectral group of the NATO. He has recently coauthored a number of papers presented in the field of hydrology at events such as the *ESA Livng Planet Symposium* (2019), the *Earth Observation for Water Cycle Science 2020* (ESA, GEWEX) in 2020, and soon in *HYDROSPACE-GEOGloWS 2021 (ESA-ESRIN)* in Frascati, Italy, in 2021. Since 2008, he has been a Senior Consultant and responsible for radar activities within the Skill Center Image processing of the Space Business Unit of CS GROUP - France in Toulouse facilities (France). He is currently involved in image processing, geospatial intelligence, and user ground segment domains.

Florence Tupin (Senior Member, IEEE) received the engineering and the Ph.D. degrees in signal and image processing from Ecole Nationale Superieure des Telecommunications (ENST), Paris, France, in 1994 and 1997, respectively, and the Habilitation a Diriger des Recherches degree in imaging science from the University of Rennes, Rennes, France, in 2007.

She was with SAGEM, Paris, France, where she worked on fingerprint recognition from 1997 to 1998. She is currently a Professor of Image and Signal Processing with LTCI, Telecom Paris, Paris, France. Since 2014, she has been the Head of the Image, Modeling, Analysis, GEometry, and Synthesis Team, LTCI. She has coauthored more than 200 papers. Her research interests include image processing and analysis, especially for remote sensing and synthetic aperture radar imaging applications, and earth observation.

Dr. Tupin has been a member of several international and national technical conference committees since 2003. She was the Chair of the Urban Remote Sensing Joint Event held in Paris in 2007. She was an Associate Editor for the IEEE TRANSACTIONS ON GEOSCIENCE AND REMOTE SENSING from 2007 to 2016. She was the recipient of several awards, and among them is the IEEE GRSS Transactions Prize Paper Award in 2016 for work on nonlocal speckle filtering.